ADVANCED FUNCTIONAL MATERIALS
www.afm-journal.de

Unraveling Loss Mechanisms Arising from Energy-Level Misalignment between Metal Halide Perovskites and Hole Transport Layers

*Jae Eun Lee, Silvia G. Motti, Robert D. J. Oliver, Siyu Yan, Henry J. Snaith, Michael B. Johnston, and Laura M. Herz**

Metal halide perovskites are promising light absorbers for multijunction photovoltaic applications because of their remarkable bandgap tunability, achieved through compositional mixing on the halide site. However, poor energy-level alignment at the interface between wide-bandgap mixed-halide perovskites and charge-extraction layers still causes significant losses in solar-cell performance. Here, the origin of such losses is investigated, focusing on the energy-level misalignment between the valence band maximum and the highest occupied molecular orbital (HOMO) for a commonly employed combination, $FA_{0.83}Cs_{0.17}Pb(I_{1-x}Br_x)_3$ with bromide content x ranging from 0 to 1, and poly[bis(4-phenyl)(2,4,6-trimethylphenyl)amine] (PTAA). A combination of time-resolved photoluminescence spectroscopy and numerical modeling of charge-carrier dynamics reveals that open-circuit voltage (V_{OC}) losses associated with a rising energy-level misalignment derive from increasing accumulation of holes in the HOMO of PTAA, which then subsequently recombine non-radiatively across the interface via interfacial defects. Simulations assuming an ideal choice of hole-transport material to pair with $FA_{0.83}Cs_{0.17}Pb(I_{1-x}Br_x)_3$ show that such V_{OC} losses originating from energy-level misalignment can be reduced by up to 70 mV. These findings highlight the urgent need for tailored charge-extraction materials exhibiting improved energy-level alignment with wide-bandgap mixed-halide perovskites to enable solar cells with improved power conversion efficiencies.

1. Introduction

Metal halide perovskites (MHPs) have been in the limelight as light-harvesting materials in next-generation "perovskite" solar cells that have demonstrated an unprecedentedly rapid improvement. Their certified power conversion efficiencies (PCE) have risen to 26.1% over the past decade, approaching the record efficiency of crystalline silicon (c-Si).[1] Such success derives from their excellent optoelectronic properties including high optical absorption coefficients near 10^5 cm^{-1},[2] sharp absorption edges with Urbach energies as small as 15 meV,[3] low exciton binding energies similar to thermal energy at ambient temperature,[4] sufficiently slow electron-hole recombination rates of $\approx 10^{-10}$ $cm^3 s^{-1}$,[5] relatively low defect densities even for materials processed with simple solution or evaporation methods,[6] and long charge-carrier diffusion lengths of a few μm.[7] In addition, the ease of bandgap tunability of lead mixed-halide perovskites from ≈1.5–2.3 eV through

J. E. Lee, S. G. Motti, R. D. J. Oliver, S. Yan, H. J. Snaith, M. B. Johnston, L. M. Herz
Department of Physics
Clarendon Laboratory
University of Oxford
Parks Road, Oxford OX1 3PU, UK
E-mail: laura.herz@physics.ox.ac.uk

The ORCID identification number(s) for the author(s) of this article can be found under https://doi.org/10.1002/adfm.202401052

DOI: 10.1002/adfm.202401052

S. G. Motti
School of Physics and Astronomy
Faculty of Engineering and Physical Sciences
University of Southampton
University Road, Southampton SO17 1BJ, UK

R. D. J. Oliver
Department of Physics and Astronomy
University of Sheffield
Hicks Building, Hounsfield Road, Sheffield S3 7RH, UK

L. M. Herz
Institute for Advanced Study
Technical University of Munich
Lichtenbergstrasse 2a, D-85748 Garching, Germany

simple adjustment of the ratio between iodide and bromide on the X site of the ABX_3 crystal makes them particularly appealing for use in multijunction solar cells.[8] For example, c-Si:MHP tandem solar cells are theoretically capable of achieving a PCE of 45.3%,[9] significantly surpassing the thermodynamic limit of a single-junction solar cell.[10] However, the actual record PCE reported for state-of-the-art c-Si:MHP tandem solar cells is currently only 33.9%,[1] highlighting that significant losses persist.

One of the main challenges of two-terminal tandem solar cells is to ensure current-matching between the subcells while maximizing open-circuit voltages (V_{OC}) of each subcell in order to optimize overall PCE.[9] Such current matching requires careful choice of the bandgaps of the constituent semiconductors. Since the bandgap of c-Si in the bottom cell is fixed, this necessitates tuning of the perovskite top cell in order to achieve a wide-bandgap perovskite (WBP) with a bandgap greater than 1.7 eV. However, it has been widely observed that the average V_{OC} losses increase with increasing bandgap when identical transport layers are used.[9b,11] Identifying the cause of such loss mechanisms in WBPs has therefore emerged as a prominent challenge toward the goal of achieving high-performance silicon-perovksite tandem solar cells. Several key factors affecting V_{OC} losses in WBPs have been identified, including bulk non-radiative losses, interfacial losses, and halide segregation under illumination or electric bias, during which the initial mixed iodide and bromide phases segregate to form iodide-rich and bromide-rich phases.[9b,11b,12] Initially, halide segregation was suspected to be the main source of V_{OC} losses because the formation of the iodide-rich phases with a narrower bandgap,[12b] and channeling of charge carriers into these phases,[12c] would ultimately limit the quasi-fermi level splitting (QFLS) to a lower value than that achievable in the original mixed-halide material. However, recent research instead stipulated that non-radiative losses occurring at the interface between the MHP and transport layers are a far more prominent source of losses than those arising from halide segregation.[9b,11b] Through the development of novel transport layers with better energy-level alignment, surface passivation techniques, and fabrication process methods, a state-of-the-art ≈1.7 eV WBP has recently managed to achieve a V_{OC} of just over ≈1.3 V, corresponding to ≈80 mV of V_{OC} loss with respect to the Shockley-Queisser limit.[13] Notably, this substantial increase in V_{OC} was realized through a treatment based on 1,3-propane-diammonium iodide (PDA), which significantly reduces V_{OC} losses originating from the WBP:C60 interface.[13a] In this case, the losses occurring at the WBP:hole transport layer (HTL) interface becomes the limiting factor on which further improvement must focus.[11b,14] Importantly, such losses at WBP:HTL interfaces will become even more significant for a 2 eV bandgap WBP, which offers an ideal bandgap for the top cell in perovskite/perovskite/c-Si triple junction solar cells.[11a,15] Therefore, in order for WBPs and the associated tandem solar cells to reach their full potential, an understanding and mitigation of the interfacial losses at the WBP:HTL interface will be critical. However, the extent of interfacial losses with increasing energy-level misalignment and their link with charge-carrier dynamics as well as the resulting loss mechanisms have not been fully understood.[11c,12a,14b,16]

In this work, we investigate the photophysical origin of losses at the interfaces between films of the prototypical WBP $FA_{0.83}Cs_{0.17}Pb(I_{1-x}Br_x)_3$ with bromide content varying $0 \leq x \leq 1$ and the frequently implemented HTL poly[bis(4-phenyl)(2,4,6-trimethylphenyl)amine] (PTAA). We explore how such interfacial losses depend on the varying energy-level misalignment between the valence band maxima (VBM) of the WBPs and the highest occupying molecular orbital (HOMO) of PTAA by applying a global kinetic model based on experimentally recorded time-resolved photoluminescence (TRPL) decays. $FA_{0.83}Cs_{0.17}Pb(I_{1-x}Br_x)_3$ thin films were coated with either PTAA, or poly(methyl methacrylate) (PMMA) as an inert reference, and characterized through X-ray diffraction, optical absorption, photoluminescence, and THz conductivity probes, to ascertain that representative high-quality MHPs had been fabricated across the different bromide contents. We show through a combination of steady-state PL and TRPL that the presence of a PTAA hole-extraction layer introduces additional non-radiative recombination processes which become more significant with increasing energy-level misalignment with the WBP. We develop a kinetic model that includes a range of dynamical charge-carrier processes occurring at the MHP:PTAA interface, such as hole transfer, hole back transfer, and across-interfacial recombination. Through a correlation of such global modeling with experimental TRPL traces, we reveal that the combination of an increasing degree of hole accumulation, which is defined as the ratio of hole transfer rate to hole back transfer rate, and subsequent across-interfacial recombination significantly enhance non-radiative losses with increasing energy-level misalignment. We show that while the early TRPL dynamics are mainly influenced by hole transfer to the HOMO of PTAA, the later TRPL dynamics are determined by across-interfacial recombination with the amplitude of the late TRPL dynamics determined by the degree of hole accumulation. We further quantitatively assess the extent to which defect-assisted recombination contributes to the dynamics. Based on such complete mapping of individual dynamic processes followed by charge carriers in time, we identify that for the scenario of an ideally matched HTL, elimination of such loss processes could recover V_{OC} losses by 41 and 70 mV for 1.7 and 2.0 eV MHPs, respectively. Our findings provide essential fundamental understanding of the dominant non-radiative losses currently occurring at the interface of WBPs with hole extraction layers and pave the way for the design and development of more suitable HTLs with ideal energy-level alignment.

2. Results and Discussion

2.1. Optoelectronic Properties of $FA_{0.83}Cs_{0.17}Pb(I_{1-x}Br_x)_3$

Thin films of $FA_{0.83}Cs_{0.17}Pb(I_{1-x}Br_x)_3$ with bromide content x ranging from 0 to 1 with an increment of 0.1 were fabricated through a solution-casting method, as described in Section S1 (Supporting Information), and subsequently coated with a film of either PMMA or PTAA. While PMMA acts as an electronically inert encapsulating layer preventing accelerated degradation, e.g. induced by moisture or air under illumination,[12d,e,19] PTAA acts as a HTL, which has proven to work well across the full compositional range investigated.[11a,c,12d,16c,18] The structure of such "half stack" architectures is schematically shown in the inset of **Figure 1a**. To illustrate the electronic alignment at the MHP:PTAA interfaces, Figure 1a shows the band edge

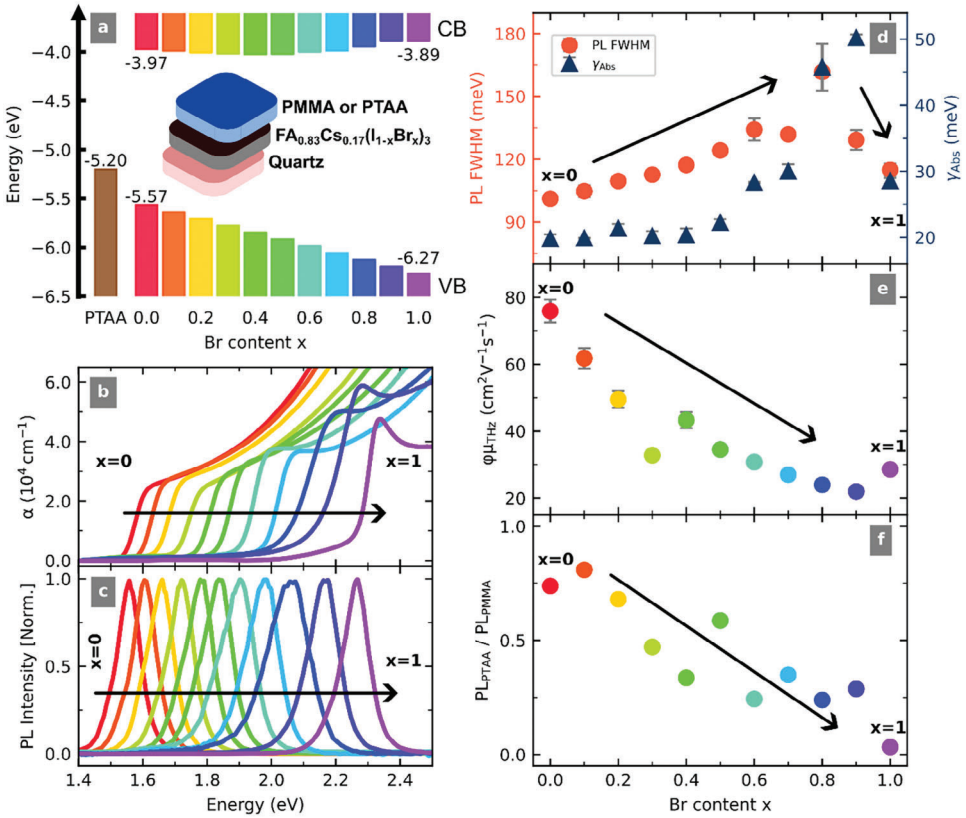

Figure 1. Bulk optoelectronic properties of $FA_{0.83}Cs_{0.17}Pb(I_{1-x}Br_x)_3$ for a range of bromide contents x ranging from 0 (red) to 1 (purple). a) Schematic energy level diagram for the MHP:PTAA interface, showing the range of valence band maxima (VBM) and conduction band minima (CBM) energies for $FA_{0.83}Cs_{0.17}Pb(I_{1-x}Br_x)_3$ and the HOMO level of PTAA (brown). Energy values for the VBM of MHPs were obtained by extrapolating the ultraviolet photoelectron spectroscopy (UPS) measurements obtained from Prathapani et al.[17] (see Section S5 in Supporting Information for further details) with the CBM obtained through addition of the bandgap energies to VBMs for each Br content (see Section S4.2.2 in Supporting Information). The HOMO of PTAA is taken as the value reported by Endres et al.[18] The inset shows the bilayer structure of $FA_{0.83}Cs_{0.17}Pb(I_{1-x}Br_x)_3$ thin films coated with either PMMA or PTAA. b) Absorption coefficients (α) of $FA_{0.83}Cs_{0.17}Pb(I_{1-x}Br_x)_3$ coated with PMMA across Br contents x. c) Normalized steady-state PL across Br contents x. d) Corresponding full width at half maximum of the PL spectra (PL FWHM) (see Section S6 in Supporting Information) and absorption edge broadening parameter (γ_{Abs}) (see Section S4.2 in Supporting Information). f) Effective THz electron-hole sum mobility ($\varphi\mu_{THz}$) where φ is the photon-to-charge branching ratio and μ_{THz} is the sum mobility for the PMMA-coated MHP films with different Br contents x (see Section S8.1 in Supporting Information). d) Ratio of the spectrally integrated PL emerging from the PTAA-coated MHP films to that emerging from the PMMA-coated MHP films, determined as a function of Br contents x.

energies for $FA_{0.83}Cs_{0.17}Pb(I_{1-x}Br_x)_3$ together with the HOMO of PTAA, illustrating that with increasing x, the valence band maximum (VBM) of $FA_{0.83}Cs_{0.17}Pb(I_{1-x}Br_x)_3$ deepens with respect to the vacuum level while the conduction band minimum (CBM) changes relatively little. Thus, increasing x leads to a greater energetic offset between the HOMO of PTAA and the VBM of $FA_{0.83}Cs_{0.17}Pb(I_{1-x}Br_x)_3$,[17] which allows a systematic examination of the effect of such band offsets for an unaltered chemical structure of the molecular HTL. Such trends have been well established across both theoretical and experimental literature reports.[17,20] for lead iodide-bromide perovskites. The position of the VBM has been shown to be influenced by the hybridization between the 6*s* state of Pb and n*p* state of the halides with a dominant contribution from the n*p* states of the halides.[20a,b,d] When I is substituted with Br, the n*p* state shifts downwards with increasing electronegativity deepening the VBM relative to the vacuum level. In contrast, the CBM is dominantly influenced by the 6*p* state of Pb, and changes in halide content thus have minimal effect on the CBM.[20a,b,d] With general consensus across literature reports for such mixed-halide perovskites,[17,20] we here utilize values for the VBM reported previously from ultraviolet photoelectron spectroscopy (UPS) measurements by Prathapani et al.[17] for the specific compositional range we investigate (see Section S5, Supporting Information for further details). Values shown for the CBM were determined by us through the addition of the optical bandgap energies calculated from Elliot fits to the absorption coefficient spectra (see Section S4.2.2 in Supporting Information). The HOMO energy level of PTAA is taken from previously reported UPS measurements by Endres et al.[18]

We further characterized the basic structural and optoelectronic properties of the $FA_{0.83}Cs_{0.17}Pb(I_{1-x}Br_x)_3$ films, confirming that these are indeed high-quality representatives and that the intended x has been incorporated for each thin film. Gradual blue shifts in the absorption edges and PL spectra, as shown in Figure 1b,c respectively, indicate that the expected increasing bromide content has been incorporated.[8,17,21] X-ray diffraction

(XRD) data display the relevant XRD peaks, together with those of typical impurities, which do not affect our analysis significantly (See Section S3 in Supporting Information). The perovskite diffraction peaks show a gradual increase in 2θ with increasing x, indicating lattice contraction induced by the replacement of larger iodide ions by smaller bromide ions.[8,12e,17] We further examine optoelectronic quality across the perovskite series with increasing bromide content. We find that both the full width at half maximum of the photoluminescence (PL FWHM) and the absorption edge broadening parameter (γ_{Abs}) as illustrated in Figure 1d increase with increasing x (see Sections S6 and S4.2 in Supporting Information respectively). In addition, the effective electron-hole sum mobilities at THz frequencies ($\varphi\mu_{THz}$) as shown in Figure 1e decrease with increasing bromide content. While such trends may partly be influenced by an increase in electron-phonon coupling with increasing bromide content, driven by the increasingly polar lead-halide bond,[22] they may also be significantly influenced by extrinsic factors, such as scattering deriving from disorder, defects, and other imperfection that increase toward the high-bromide content MHPs, similar to previous reports.[17,23]

To investigate the impact of the HTL on the overall optoelectronic quality of the half-stack architectures, Figure 1f shows the ratio between the spectrally integrated steady-state PL intensity recorded for the PTAA-coated MHP and that for the inert PMMA-coated MHP (PL_{PTAA}/PL_{PMMA}). The observed decrease in PL_{PTAA}/PL_{PMMA} with increasing bromide content x indicates that PTAA introduces significant additional non-radiative losses, compared to the PMMA-coated thin films, that grow markedly with increasing bromide content. According to detailed-balance theory,[11b,12a,24] such additional non-radiative losses introduced by PTAA will detrimentally lower the V_{OC} with respect to the MHP bandgap. To understand the role of the MHP:PTAA interface in such non-radiative losses and the reasons for their growth with increasing bromide content, we examine the charge-carrier dynamics occurring at such interfaces, assessing a complete set of dynamic processes.

2.2. Charge-Carrier Dynamics

We recorded the time-resolved photoluminescence transients for both PMMA- and PTAA-coated MHP films across the full bromide content range, using the time-correlated single photon counting (TCSPC) technique. Pulsed excitation was carried out at a wavelength of 470 nm to prevent parasitic absorption and charge generation in the PMMA or PTAA layers,[18] which would further complicate the analysis of charge-carrier dynamics. An excitation pulse fluence of 76 nJcm^{-2} was chosen, which is roughly equivalent to 1-sun intensity, injecting an initial charge-carrier density of $\approx 10^{15}$ cm^{-3}. We ascertained that halide segregation effects, which iodide-bromide perovskites with mid- to high-bromide content are liable to exhibit,[12b,h,25] had an insignificant effect on those transients, under these excitation conditions with TRPL acquisition time limited to 1 minute (see Section S7.6 in Supporting Information).

Representative TRPL decay dynamics are shown in **Figure 2** for the thin films of the $FA_{0.83}Cs_{0.17}Pb(I_{1-x}Br_x)_3$ with bromide content of x = 0, 0.2, and 1 (see Section S7.3 in Supporting Information for the full dataset recorded across the whole composition range). We observe that the MHP films coated with the inert PMMA layers exhibit mostly monoexponential PL decays (orange circles), which is in agreement with charge-carrier recombination dominated by defect-assisted pathways at sufficiently low charge-carrier densities.[26] However, PTAA-coated MHP films exhibit two distinct regimes in the PL transients (blue triangles), where an initial fast decay occurring within the first 100 ns is followed by a late slow decay occurring over the hundreds of ns. The

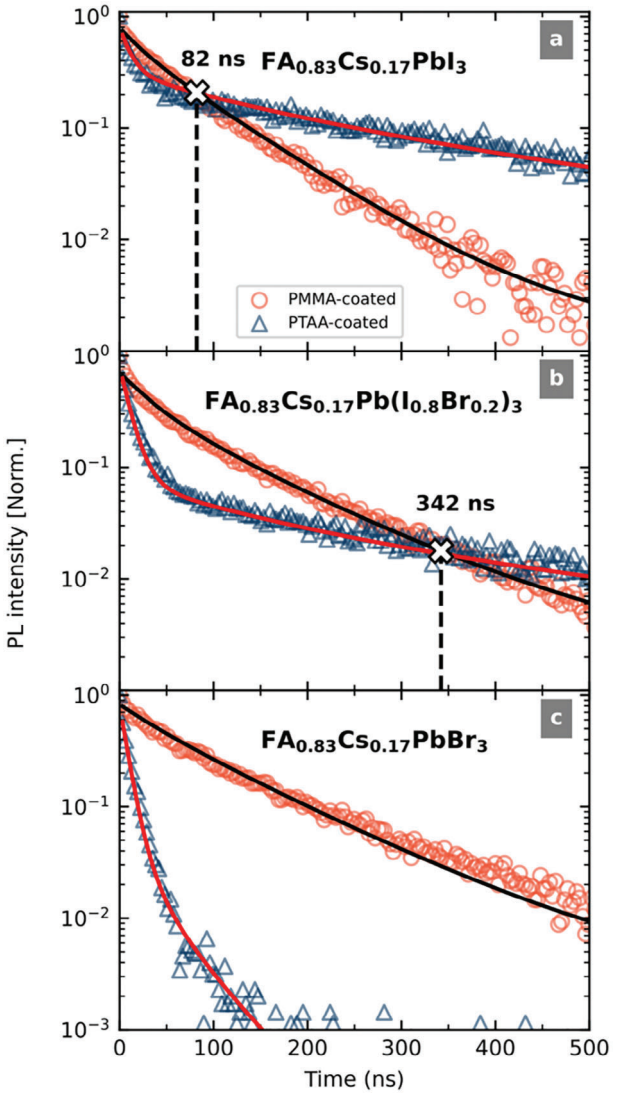

Figure 2. Time-resolved photoluminescence, measured with the time-correlated single photon counting (TCSPC) method, for $FA_{0.83}Cs_{0.17}Pb(I_{1-x}Br_x)_3$ with bromide content of a) x = 0, b) x = 0.2 and c) x = 1, coated with either a PMMA (orange circles) or a PTAA (blue triangles) film. PL transients were recorded following excitation with a pulse fluence of 76 nJcm^{-2} and a wavelength of 470 nm, originating from a diode laser with a repetition rate of 1 MHz. Best fits of the kinetic model described in the text are plotted together in black and red solid lines for the PMMA- and PTAA-coated thin films respectively. The "crossover point" is indicated with a black-edged white cross and label stating its intersection time. Transients for the full composition range are shown in Section S7.3 (Supporting Information).

sufficiently different shapes of the transients recorded for PMMA- and PTAA-coated MHP films lead to a "crossover point" between the two transients for most MHP compositions, as indicated in Figure 2 by the black-edged white crosses.

The distinct shape of the transients recorded for MHP films in the presence of the PTAA HTL layers, and its deviation from simple monoexponential decay suggest that in the presence of PTAA, extra dynamic pathways are introduced in addition to the simple bulk defect-assisted recombination present in the PMMA-coated MHP. As Figure. 2 shows, an increase in bromide content of the PTAA-coated MHP from x = 0 to x = 0.2 accelerates the early fast decay and delays the "crossover point" from 82 ns to 342 ns. As we show through detailed modeling later, such early-time fast decays are influenced by hole transfer to the PTAA layer and non-radiative recombination. When the bromide content is increased further from x = 0.2 to x = 1, both early and late decays become even more dominant, leading to an absence of the "crossover point". We note that such shortening of both early and late PL decays with increasing bromide content is congruent with the decrease in the PL ratios (PL_{PTAA}/PL_{PMMA}) shown in Figure 1f, demonstrating that the MHP:PTAA interface introduces additional non-radiative loss channels that become more prominent with increasing bromide content in the MHP. As such, the "crossover point" between transients recorded for the MHP:PTAA interface and those recorded for the interface with electronically inert PMMA can therefore serve as an intuitive figure of merit to quantify the degree of additional non-radiative losses arising from the PTAA interface. As we show through detailed modeling below, holes transferred from the MHP to PTAA may ultimately slowly return to the MHP, leading to the delayed luminescence decay rates observed for MHP:PTAA architectures at long times after excitation. However, if such a return of holes is prevented by an energetic barrier and excessive non-radiative recombination losses across the interface, delayed PL in the MHP will be inhibited and the two curves will no longer cross. As such, the absence of "crossover points" is therefore a clear indicator of detrimental and dominant non-radiative recombination across the interface, unraveled in detail in our model described below.

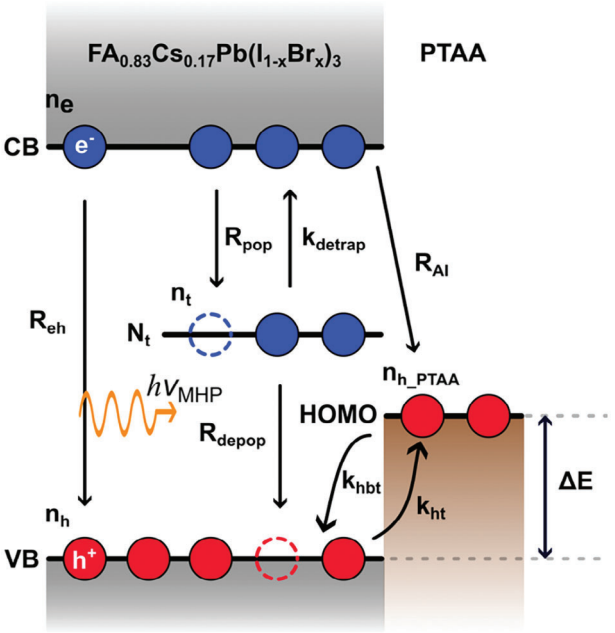

Figure 3. Schematic diagram illustrating the dynamical processes occurring in a bilayer stack of $FA_{0.83}Cs_{0.17}Pb(I_{1-x}Br_x)_3$ and PTAA, described by the kinetic model. Upon excitation, electrons (blue solid circles) with density n_e are generated in the conduction band (CB) and an equal number of holes (red solid circles) are generated with density n_h in the valence band (VB). Electrons and holes may undergo band-to-band radiative bimolecular recombination with a rate constant R_{eh}. Alternatively, electrons in the CB may be trapped in the available defect states (dotted empty blue circles) with a rate constant R_{pop} and subsequently recombine with holes in the VB with a rate constant R_{depop}. The total density of defects is N_t, and that of electrons occupying defects is n_t. Trapped electrons may return to the CB with a rate k_{detrap}. A fraction of holes in the VB may be transferred to the HOMO of the PTAA layer with a rate k_{ht}, some of which may subsequently return to the VB of the MHP, with a rate k_{hbt}, or recombine with electrons in the CB of the MHP with a rate constant R_{Al}. The density of holes in the HOMO of the PTAA is described by n_{h_PTAA}. ΔE is the energy offset between the VBM of $FA_{0.83}Cs_{0.17}Pb(I_{1-x}Br_x)_3$ and the HOMO of PTAA ($\Delta E = E_{HOMO} - E_{VBM}$). $h\nu_{MHP}$ represents photoluminescence from the MHP and is explicitly shown to indicate that the only radiative recombination results from band-to-band transitions within the MHP.

2.3. Modelling TCSPC Decays

In order to understand the losses introduced at the MHP:PTAA interface, we consider a comprehensive set of photophysical processes that contribute to the charge-carrier dynamics in such half stacks, as illustrated schematically in **Figure 3**. Upon photoexcitation, an equal number of electrons and holes are generated in the conduction band (CB) and valence band (VB) of the MHP and quickly thermalize to their respective band edges. The resulting density of excited electrons in the CB (n_e) undergoes various recombination processes, including (i) band-to-band radiative bimolecular recombination with the holes in the VB, (ii) capture into defect states located either in the bulk or at the surface of MHP, (iii) recombination across the MHP:PTAA with the holes that had previously been transferred to the HOMO of PTAA. We do not include Auger recombination here because it is only significant at charge-carrier densities $\approx 10^{18}$ cm^{-3} (see Section S8.4 in Supporting Information), much higher than those present under solar illumination and those injected under the fluences implemented here.[26] Charge-carrier traps may potentially be filled at high excitation densities, which is counteracted by trapped charge carriers, such as electrons shown here, recombining with holes in the VB. These trapped electrons may subsequently return to the CB. In addition, photogenerated holes in the VB of the MHP (n_h) may transfer to the HOMO of PTAA, a portion of which may gradually return back to the VB of the MHP. In our model, we neglect the effect of band bending at the MHP:PTAA interface in the dark as a first approximation, given that the Fermi levels of $FA_{0.83}Cs_{0.17}Pb(I_{1-x}Br_x)_3$ across x are fairly well aligned with those of PTAA.[17,20a] In addition, we note that electron transfer to the LUMO of PTAA is considered to be highly unlikely owing to the high energetic barrier $\approx$2.2 eV and therefore not included in the model.[18,27] While we limit our examination to the relevant example of $FA_{0.83}Cs_{0.17}Pb(I_{1-x}Br_x)_3$:PTAA bilayers, the mechanisms described generally occur at any MHP interfaced with a charge transport layer.[28]

In past literature reports, various approaches have been employed to describe the dynamics of charge-carrier recombination at the interface between MHPs and charge transport layers (CTL). As a simple approach, the charge-carrier loss at the interface has been quantified as surface recombination velocity (SRV) by comparing the average recombination lifetimes of a passivated MHP without and with a CTL present.[29] SRV is a useful figure of merit for a quick quantification of the surface recombination introduced by an interface, but it is unable to distinguish and disentangle the various charge-carrier recombination processes mentioned above.[16c,29,30] On the other hand, such losses can be quantified within a more detailed drift-diffusion model, including transport and Poisson equations.[31] Such models have been successfully used to describe and quantify the origin of Voc losses at an interface, but they tend to be too complex and multi-parameterized to allow the extraction of reliable parameters from fits to the TRPL decays. As a compromise, Hutter et al. have successfully used coupled differential equations to quantify and decouple individual charge-carrier dynamics in the bulk as well as the interface of MHPs.[32] We believe that the level of complexity provided by such rate equation models is suitable for our analysis, given that charge diffusion and Poisson effects are minimal for the conditions under which experiments were carried out here (see Section S7.12 in the Supporting information for details).

Therefore, we provide a comprehensive description of the charge-carrier processes in a MHP:PTAA bilayer, by applying the following set of couple differential equations, whose solutions we fit to the experimental PL transients in order to decouple and quantify each process:

$$\frac{dn_e(t)}{dt} = -R_{eh} n_e(t)\, n_h(t) - R_{pop}\left(N_t - n_t(t)\right) n_e(t) - R_{AI} n_e(t)\, n_{h\_PTAA}(t) + k_{detrap} n_t(t) \quad (1)$$

$$\frac{dn_h(t)}{dt} = -R_{eh} n_e(t)\, n_h(t) - R_{depop} n_t(t)\, n_h(t) - k_{ht} n_h(t) + k_{hbt} n_{h\_PTAA}(t) \quad (2)$$

$$\frac{dn_t(t)}{dt} = R_{pop}\left(N_t - n_t(t)\right) n_e(t) - R_{depop} n_t(t)\, n_h(t) - k_{detrap} n_t(t) \quad (3)$$

$$\frac{dn_{h\_PTAA}(t)}{dt} = k_{ht} n_h(t) - k_{hbt} n_{h\_PTAA}(t) - R_{AI} n_e(t)\, n_{h\_PTAA}(t) \quad (4)$$

$$PL(t) = R_{eh} n_e(t)\, n_h(t) \quad (5)$$

Here, $n_e(t)$, $n_t(t)$, $n_h(t)$ and $n_{h\_PTAA}(t)$ are the time-dependent densities of electrons in the CB or in defect states of the MHP, the densities of holes in the VB of the MHP, or in the HOMO of PTAA respectively. N_t is the total density of defects (filled or unfilled) in the MHP, R_{pop} is the rate at which these defects are being populated with electrons and R_{depop} is the rate with which they are being depopulated through recombination with holes in the VB of the MHP. k_{detrap} is the rate of trapped electrons returning to the CB of the MHP. k_{ht} is the rate of hole transfer from MHP to PTAA, while k_{hbt} is the rate with which these holes transfer back from PTAA into the MHP. R_{AI} describes the rate with which holes in PTAA recombine non-radiatively across the interface with electrons in the CB of the MHP.

We solve Equations 1, 2, 3, and 4 in order to obtain $n_e(t)$, $n_h(t)$, $n_t(t)$ and $n_{h\_PTAA}(t)$ respectively. Model TRPL decays are derived from these quantities through Equation 5. Optimised output parameters are then obtained from fits of Equations 1, 2, 3, 4, and 5 to TRPL decays globally across a range of fluences (see Section S7 in Supporting Information). We note that the bimolecular electron-hole recombination rate constant R_{eh} is obtained (see Section S8.2 in Supporting Information) and fixed prior to this through global fits to fluence-dependent optical-pump terahertz-probe (OPTP) photoconductivity transients which are able to record this second-order effect more accurately owing to higher pulsed excitation fluences.[5,22a] To achieve high accuracy of resulting output parameters, we follow a two-step process, first determining a subset of parameters for the MHP coated with the electronically inert layer PMMA to determine MHP-specific processes, then using these as inputs to describe the MHP:PTAA bilayer. Specifically, for TRPL transients recorded for the PMMA-coated MHP films, k_{ht} k_{hbt} and R_{AI} are set to zero and R_{pop}, R_{depop}, k_{detrap} and N_t are obtained from the model (see Section S7.4 in Supporting Information). Subsequently, transients for the PTAA-coated MHP films are fitted by fixing R_{pop}, R_{depop} and k_{detrap} to the values obtained from the PMMA-coated MHP films for each bromide content. Thus, we assume that the nature of the electron defects in the MHP is similar for both PMMA and PTAA-coated MHP films, which is a fair assumption given that these MHP films are coated through the same process and their bulk optoelectronic properties appear identical (see Sections S3,S4, and S6 in Supporting Information). However, the exact density of defects present in the MHP may differ somewhat owing to different polymer interfaces and N_t is thus allowed to be varied. Moreover, for fits to transients recorded for MHP:PTAA films, k_{ht}, k_{hbt} and R_{AI} are also set as free parameters, given that these processes are significant in this case. Full details and a summary of the assumptions made for the model are presented in Section S7.2 of Supporting Information.

Our model reproduces the experimental data with excellent accuracy as seen by the superimposed fits plotted as solid lines in Figure 2 (see Figures S21 and S22 in Supporting Information for other compositions). From the modeled dynamics, we extract important rate constants summarized in **Figure 4**, which shows these parameters either as a function of increasing bromide content, or versus the corresponding increase in band offset between the VBM of the MHP and the HOMO of PTAA ($\Delta E = E_{HOMO} - E_{VBM}$).

Figure 4a shows that an increase in Br content x leads to a higher density of defects N_t in the PTAA-coated $FA_{0.83}Cs_{0.17}Pb(I_{1-x}Br_x)_3$ films, both for the PMMA- and PTAA-coated films (see Figure S23 in Supporting Information for N_t of the PMMA-coated films). This finding is consistent with our characterization of bulk optoelectronic properties described above in Section 2.1 and with previous literature reports.[8,17,23] It is worth noting that while N_t describes the density of defects in the MHP, it does not discriminate whether these are located in the bulk or at the surface or grain boundaries of the MHP.

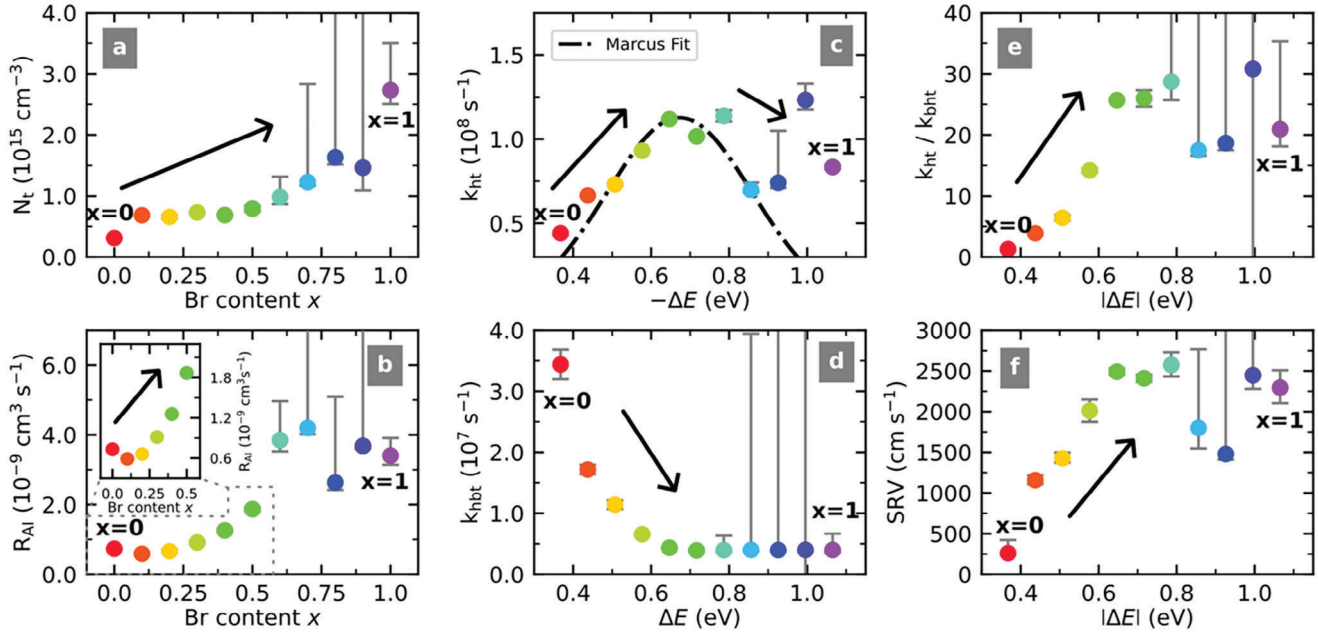

Figure 4. a–d) Parameters obtained from global fits of the kinetic model to experimentally recorded TRPL transients for $FA_{0.83}Cs_{0.17}Pb(I_{1-x}Br_x)_3$ films coated with PTAA for a range of Br contents x; a) total defect density (N_t), b) across-interfacial recombination rate constant (R_{AI}), c) hole transfer rate (k_{ht}) from the MHP to PTAA and d) hole back transfer rate (k_{hbt}) from PTAA to the MHP. The inset in b) shows the zoomed-in region between x = 0 and x = 0.5. The details of the fittings can be found in Section S7.2 (Supporting Information). e) Ratio of k_{ht} to k_{hbt} representing the degree of hole accumulation with increasing x. f) Surface recombination velocity (SRV) with increasing x (see Section S7.9, Supporting Information for calculation details). For a,b), and d–f), the large error bars indicate the region of bromide content from which the initial TRPL signal decay becomes so prominent that the fits to the late, slow dynamics dominated by hole back transfer and across-interface recombination are determined with lower accuracy. c–f) are plotted against energy level offset ($\Delta E = E_{HOMO} - E_{VBM}$) to explicitly illustrate the impact of ΔE. $-\Delta E$ in c) indicates energetically favorable energy offset for hole transfer. ΔE in d) indicates energetically unfavourable energy offset for hole back transfer. $|\Delta E|$ in e,f) represents the absolute energy offset. The arrows are guides to illustrate trends in the data.

We further examine the dependence of the across-interfacial recombination rate constant R_{AI}, which describes the non-radiative recombination of electrons at the CBM of the MHP with holes transferred to the HOMO of PTAA. Figure 4b shows that R_{AI} increases monotonically with increasing bromide content x. We note that the values of R_{AI} for x ≥ 0.6 are difficult to interpret because for these compositions, the late decay (>100 ns) only makes a relatively small contribution to the PL amplitude within the acquisition time, which is limited to 1 minute to avoid halide segregation (see Section S7.6 in Supporting Information). Given that the energy offset bridged by this recombination step is not ΔE but rather the difference between the CBM of the MHP and the HOMO of PTAA which remain relatively unchanged with bromide content (see schematic in Figure 1a), from energetic concerns alone, a relatively constant R_{AI} would be expected. However, R_{AI} extracted from the model shows a clear increasing trend with increasing x, meaning that R_{AI} involves factors other than energetic considerations. We instead propose that such across-interfacial recombination may instead originate from an increase in defect density near the MHP:PTAA interface with increasing x. The propensity for across-interfacial recombination thus seems to correlate well with that of general trap-mediated recombination observed for the MHP layer alone (Figure 4a) suggesting that a generally defective MHP will also translate into more defective interface with PTAA. Such presence of defect-mediated across-interfacial recombination has been also proposed for MHPs with different electron transport layers.[28b,33] An accurate quantification of buried defects at the interface is an extremely difficult task and therefore beyond the scope of this research. However, we stipulate that defects in the MHP of MHP:PTAA bilayers may have a tendency to form more prominently near surfaces and grain boundaries, which will offer particularly effective recombination channels to opposite charge carriers located in a charge-extraction layer in close proximity.

We continue by examining the rates of hole transfer rate k_{ht}, hole back transfer rate k_{hbt} and their ratio. Since these parameters likely depend sensitively on the band offset ΔE between the VBM of the MHP and the HOMO of PTAA, they are shown in Figure 4c,d, and e as a function of ΔE rather than bromide content x in the MHP. The values of k_{ht} shown in Figure 4c are comparable in magnitude to charge transfer rates obtained for a range of MHPs from other spectroscopic techniques such as transient microwave conductivity, surface photovoltage, and absorption spectroscopy.[32,34] As expected, with increasing energy level offset, hole transfer initially becomes energetically favorable, leading to a faster hole transfer rate with increasing bromide content up to x = 0.6 (Figure 4c). However, for higher bromide content increasing beyond x ≥ 0.6, surprisingly, k_{ht} does not seem to increase as expected, showing that any further increase in the energy level offset can no longer enhance hole transfer further. This phenomenon appears analogous to the Marcus inverted region for which a large $-\Delta E$ that might intuitively expect

to be energetically favourable actually leads to a decrease in charge transfer rates.[35] It is worth noting that k_{ht} only contributes to the early TRPL dynamics and therefore it is less affected by low PL amplitudes of later dynamics even for high bromide content MHPs. This is reflected by the error bars for extracted parameters shown in Figure 4: while errors for parameters such as N_t, k_{hbt} and R_{AI} that depend critically on the PL at later times after excitation become very large for high bromide content, those for that k_{ht}, which depends largely on the initial PL decay, are smaller, even for high bromide content. We note, however, that k_{ht} appears to deviate from the Marcus fit at larger values of $-\Delta E$ (see Section S7.8 in Supporting Information for details of Marcus fit parameters). Such deviation from the classical Marcus theory has been observed in many other systems such as molecules and quantum dots, and other models such as Marcus-Jortner-Levich[36] and Auger-assisted electron transfer[37] models have been proposed to explain such deviation. Although semi-classical Marcus models have been widely used in organic semiconductors or quantum dots where charge transport is assisted via a hopping mechanism,[35b,38] a direct application of the Marcus theory to the interface between a 3D MHP and an organic charge-transport layer has not, to our knowledge, been reported yet. While MHPs are generally assumed to exhibit bandlike transport, polymeric semiconductors are likely to display hopping transport of small polarons,[39] opening the question of whether such hopping hole transfer mechanism has relevance at the interface between MHPs and organic transport layers. Given our observations, we propose that, in this scenario, hole transfer at the MHP:PTAA interface may happen via a hopping mechanism with the interface causing a discontinuity of bandlike transport.

As a reverse process of k_{ht},[36b] the hole back transfer rate k_{hbt} extracted from our model decreases with increasing energetic barrier ΔE as shown in Figure 4d (we note that beyond x = 0.6, errors of determination increase because general non-radiative recombination becomes so strong that different processes can no longer be reliably disentangled at long times after excitation). An increase in k_{ht} and decrease in k_{hbt} with an increasing energy level offset $|\Delta E|$ and bromide content x ultimately means that more holes are being accumulated in the HOMO of PTAA with increasing $|\Delta E|$. The degree of hole accumulation can be quantified as the ratio of k_{ht} and k_{hbt} as shown in Figure 4e. We note that we have excluded a discussion of band bending at the interface because we believe that at such low fluence, the effect of electric field owing to hole accumulation is minimal, as shown by a negligible dependence of the TRPL decays on the excitation fluence for the PTAA-coated perovskite films, even as band offsets increase (See Section S7.12.2 in Supporting Information).

We further calculate corresponding values for the surface-recombination velocity based on the rate constants extracted from our model as a simple measure quantifying the degree of non-radiative dynamics at the MHP:PTAA interface (see Section S7.9 in Supporting Information for further details).[28b,29,30] Figure 4f illustrates how the SRV captures losses at the heterojunction interface arising from hole accumulation and across-interfacial recombination, which increase with increasing bromide content. The determined SRV values are comparable to those in literature reports for interfaces with similar respective band offsets.[11c,16c,29] Therefore, our kinetic model accurately reflects the observation of increasing SRV with increasing band offsets reported across the literature,[16c,29] while disentangling the contributions from different dynamic processes that lead to this effect.

2.4. Implications of Recombination Processes at the Interface on Charge-Carrier Dynamics

Having modeled such experimentally acquired curves across the series of mixed-halide perovskites, we are now in an ideal position to predict and understand the effect of increasing bromide content and therefore energy-level misalignment on the total defect densities, across-interfacial recombination, hole transfer, and hole back transfer. We thus proceed by simulating changes in each of these parameters separately, allowing us to determine clear guidelines for how such transients may be interpreted. For this purpose, **Figure** 5a–d shows simulated TRPL dynamics for a PTAA-coated $FA_{0.83}Cs_{0.17}Pb(I_{0.8}Br_{0.2})_3$ (x = 0.2) film, for which only one parameter has been varied, while all other parameters have been fixed to the values obtained from the fit to the real experimental transient, shown also again in Figure 5a–d as the black line for comparison. The x = 0.2 MHP composition was chosen here specifically as it is known to have an ideal bandgap for c-Si:MHP tandem solar cells.[9a,40]

First, we note the effect of change in defect-mediated recombination. As Figure 5a shows, an increase in the defect density (N_t) associated with the MHP results in accelerated decay of the transients, shortening both the early and late TRPL dynamics and demonstrating that defect-assisted recombination happens throughout the lifetime of charge carriers. In contrast, Figure 5b demonstrates that an increase in across-interfacial recombination rate constant R_{AI} dominantly affects the late dynamics. This is evident, as across-interfacial recombination may only become dominant once sufficient holes have been transferred to the HOMO of PTAA (see Figure S30 in Supporting Information).

Second, we examine the parameters affecting hole transfer, out and back, across the MHP:PTAA interface. Figure 5c reveals the effect of an increase in hole transfer rate k_{ht} on the TRPL dynamics. As mentioned before, an increase in the energy level offset between the VBM of the MHP and the HOMO of PTAA energetically favors hole transfer. Hole transfer depletes the density of holes in the VBM of the MHP. When k_{ht} increases, a suppressed density of holes is present in the VBM of the MHP for the given time, leading to reduced chances of band-to-band radiative bimolecular recombination with electrons in the CBM of the MHP. This results in faster early dynamics with increasing k_{ht}. Finally, Figure 5d illustrates the effect of change in the hole back transfer rate k_{hbt}. As expected, increased hole back transfer causes somewhat opposite trends to those of hole transfer, such as an increase in the amplitude of the later-time dynamics. However, it does not alter the lifetime of either the early or the late dynamics, because it is not a loss mechanism and only modulates the density of hole accumulation in the HOMO of PTAA. The intensity of the PL emerging from the PTAA-coated MHP is predominantly affected by the degree of hole accumulation in the HOMO of PTAA, because any holes present in the PTAA are highly likely to suffer from non-radiative recombination across the MHP:PTAA interface. Therefore, hole back transfer and across-interfacial

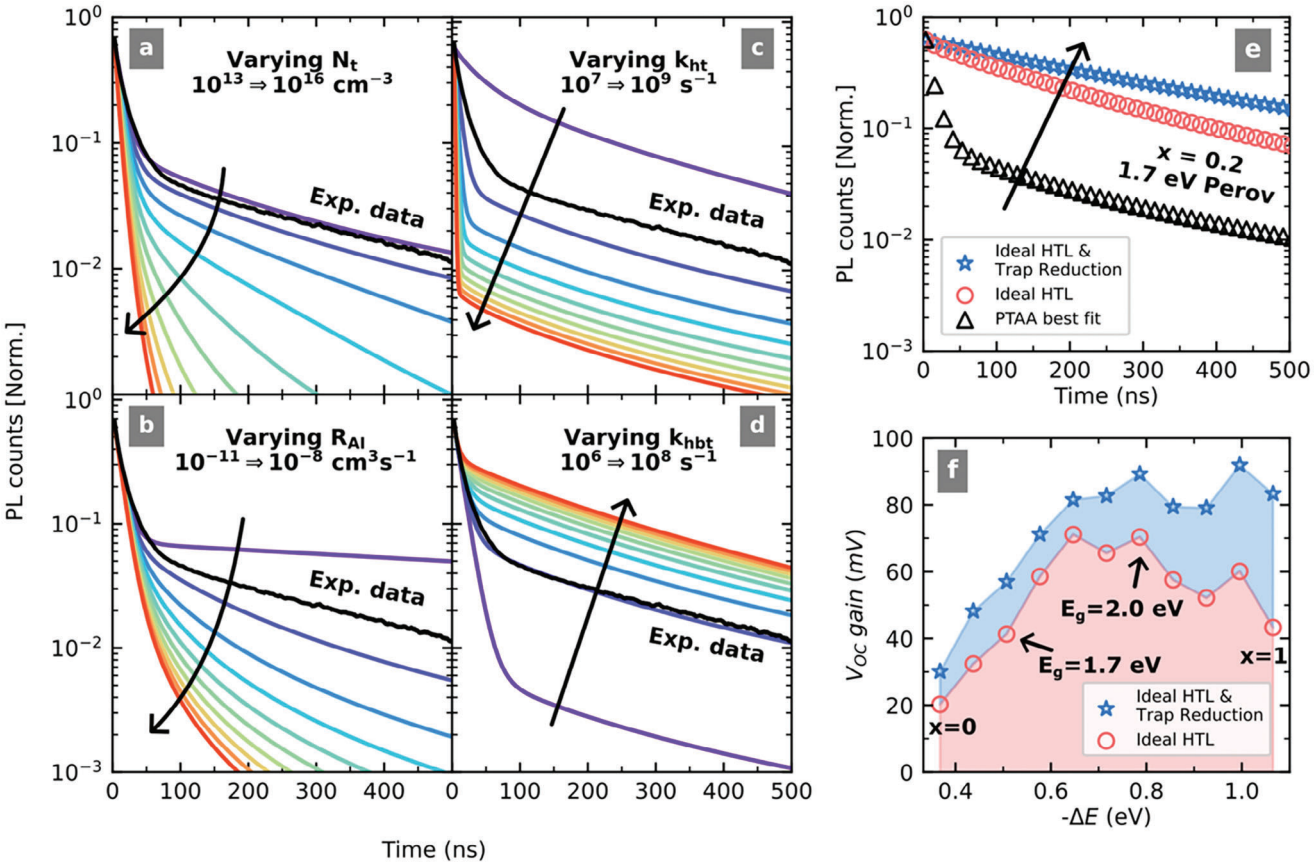

Figure 5. TRPL transients simulated through the dynamical model, assuming a) bulk trap densities (N_t) varying from 10^{13} to 10^{16} cm^{-3} in 10 evenly spaced linear increments, b) across-interface recombination rate constant (R_{AI}) varying from 10^{-11} to 10^{-8} cm^{3}s^{-1} in 10 evenly spaced linear increments, c) hole transfer rate (k_{ht}) varying from 10^7 to 10^9 s^{-1} in 10 evenly spaced linear increments and d) hole back transfer rate (k_{hbt}) varying from 10^6 to 10^8 s^{-1} in 10 evenly spaced linear increments. The gradual increase in each parameter is illustrated by the color gradient from purple to red aided by an arrow. All other parameters are fixed at those extracted from fits to the experimental TRPL transients for the film of $FA_{0.83}Cs_{0.17}Pb(I_{0.8}Br_{0.2})_3$ (x = 0.2) coated with PTAA measured at a fluence of 76 nJcm^{-2}, also plotted in black for comparison. The experimental data was refined by using a moving average of 200 points. e) Comparison between the best fit to the experimentally recorded TRPL transients at a fluence of 76 nJcm^{-2} for $FA_{0.83}Cs_{0.17}Pb(I_{0.8}Br_{0.2})_3$ coated with PTAA (black triangles) and the corresponding modeled transient for an optimized hypothetical HTL (orange circles) which has an ideal energy level offset of $|\Delta E| = 0.33 \pm 0.14$ eV and zero interfacial defects, i.e., assuming an absence of across-interfacial recombination (R_{AI}= 0 cm^{3}s^{-1}) and value of $k_{ht} = k_{hbt} = 4.45 \times 10^7$ s^{-1}, meaning that hole accumulation in the ideal HTL is eliminated ($k_{ht} - k_{hbt} = 0$ s^{-1}). The blue stars represent a modeled transient for an optimized hypothetical HTL combined with a trap reduction to $N_t = 10^{14}$ cm^{-3}. f) Open-circuit voltage (V_{OC}) gain calculated from the expected increase in radiative efficiency for an optimized hypothetical HTL (orange circles) and an optimized hypothetical HTL with reduced defect density (blue stars).

recombination are two competing processes once holes are transferred to the HOMO of PTAA, with the former boosting PL from the MHP and the latter diminishing it. Therefore, importantly, if the energy level offset is small, the hole back transfer may be sufficiently fast to minimize across-interfacial recombination and maximize PL efficiency. On the other hand, if the energy level offset is substantial, the hole back transfer is hindered by the energy barrier and accumulated holes will eventually recombine non-radiatively via across-interfacial recombination. These considerations thus highlight that optimization of the energy offset is key to enhancing PL quantum efficiency. As an aside, we note that hole back transfer is only a lossless process in open-circuit conditions for which all charge carriers ultimately must recombine, rather than being extracted. Under short circuit conditions, an increase in hole back transfer might also lead to reduced charge-carrier collection. However, we note that PL measurements on such half-stacks are always conducted under open-circuit conditions, and these closely mimic the impact on V_{OC} which is an important photovoltaic device parameter.

Overall, these simulations highlight how the TRPL dynamics of MHP:HTL bilayers are determined by a complex interplay between hole transfer, hole back transfer, and across-interfacial recombination, as well as significant trap-mediated recombination in the MHP. The early dynamics are strongly influenced by hole transfer (k_{ht}) while the late dynamics are mostly governed by across-interfacial recombination (R_{AI}). The amplitude of the late decay is determined by the interplay between out- and back-hole transfer (k_{ht} and k_{hbt}), which reflects the degree of hole accumulation. It is worth noting that while radiative electron-hole recombination (R_{eh}) does not have a significant influence on the TRPL dynamics for the low charge-carrier densities generated in this work (see Figure S54 in Supporting Information) such effects

may become more significant at higher charge-carrier densities (>10^{16} cm^{-3}) or very low trap-mediated recombination rates.[26]

Finally, we note that the relatively simple attribution of the early TRPL dynamics for MHP:HTL bilayers to solely hole transfer,[14a,16a,34a,41] and late TRPL dynamic to just across-interfacial recombination[16a,41a,c–e] can sometimes be misleading, in particular for high defect density N_t. As shown in Figure 5a, a significant increase in defect density will lead to defect-assisted recombination within the MHP becoming the dominant recombination process, which will prohibit efforts to extract reliable information about hole transfer, hole back transfer, and across-interfacial recombination through the more straightforward surface recombination velocity and differential lifetime methods previously implemented.[16c,29–31] Therefore, our model presented here provides a powerful alternative tool to analyze multi-exponential TRPL dynamics, capable of disentangling such effects and providing an overall picture of multiple processes occurring in multilayer systems comprising MHPs and their charge extraction layers.

2.5. Implications of Recombination Processes at the Interface on Device Performance

We further demonstrate how tuning of the energy-level alignment can potentially improve photovoltaic device performance by modeling charge-carrier processes for an ideally energetically matched MHP:HTL interface. Above, we established that a combination of hole accumulation and across-interfacial recombination causes non-radiative recombination at the MHP:PTAA interface. Such processes will ultimately limit the quasi-Fermi level splitting (QFLS) and consequently the V_{OC} inside a full photovoltaic device.[24,28a,42] The QFLS can be extracted from experiments by recording of the photoluminescence quantum yield (PLQY) based on the principle of detailed balance.[11b,14b,24,28a,31b,42,43] For the particular case of $FA_{0.83}Cs_{0.17}Pb(I_{0.8}Br_{0.2})_3$ (x = 0.2) examined here, the simulations shown in Figure 5e demonstrate that the TRPL lifetime can be significantly improved by replacing PTAA with such an idealized HTL, and further improvement can be realized through passivation strategies that reduce the density of traps. By using the known relationship between PLQY and QFLS, and therefore qVoc, where q is the electron charge, a corresponding increase in qVoc can be calculated from $(k_bT/q) \times \ln(PLQY_{improved}/PLQY_{pristine})$. Here, the ratio of $PLQY_{improved}$ and $PLQY_{pristine}$ was obtained from the area under TRPL decays, which provides a good estimate of the steady-state PL since it follows the same compositional trend as the integral under pulsed excitation (see Section S6 in the Supporting Information). The values calculated for qVoc through this approach are presented in Figure 5f. The orange-shaded region represents the Voc gain expected from simply replacing PTAA with an ideal HTL having an ideal energy-level alignment of $|\Delta E|$ = 0.33 ± 0.14 eV ($k_{ht} - k_{hbt} = 0\ s^{-1}$) and zero interfacial defects ($R_{AI} = 0\ cm^3s^{-1}$). The blue shaded region highlights the additional Voc gain that may be achieved by a reduction in trap density to $N_t = 10^{14}\ cm^{-3}$, e.g. through suitable passivation approaches. These trends clearly show that as $-\Delta E$ increases, the Voc loss mainly originates from the interface between the perovskite and the PTAA interface. However, for x > 0.6, the Voc loss from the interface declines owing to a slight decrease in the value of k_{ht}, while Voc losses arising from defects become more significant with increasing defect densities at higher bromide content x. We note that the compositions of x = 0.2 and x = 0.6, in particular, possess bandgaps ideal for silicon-perovskite tandem solar cells and perovskite triple junction top cells respectively.[9a,40,44] Our calculations suggest that simple optimization of the energy alignment to the HTL layer, can result in a Voc improvement by 41 and 70 mV, while additional defect passivation or reduction will increase these values to 57 and 89 mV, respectively, for these compositions. Overall, our comprehensive model encompassing all dynamical processes occurring at the interface between an MHP layer and a charge transport layer thus shows that decreasing band offsets induces a significant reduction in Voc losses at perovskite/HTL interfaces, but defect elimination or passivation may also be crucial, especially for higher bromide contents.

One might expect the scenario of $k_{ht} - k_{hbt} >> 0\ s^{-1}$ to be ideal for efficient charge extraction of holes, but we note that it will also lead to a significant decrease in PL intensity, as shown in Figure 5c, owing to hole accumulation in the HOMO of PTAA. $k_{ht} - k_{hbt} << 0\ s^{-1}$ is not an ideal condition either, despite a slight increase in radiative efficiency, because dominant hole back transfer opposes the external electric field in short-circuit conditions. (see Section S7.11 in Supporting Information for further discussion). By extrapolating k_{ht} and k_{hbt} in Figure 4c,d, we found that an ideal ΔE leading to $k_{ht} - k_{hbt} = 0\ s^{-1}$ is 0.33 ± 0.14 eV (see Section S7.11 in Supporting Information). We would like to point out that the ideal ΔE is specific to this set of MHP:PTAA bilayers studied here because under semiclassical consideration, the transfer rates will also depend on the effective density of states (DOS) and electronic coupling,[35a,36b,45] which may differ depending on the materials. However, for the general case where the effective DOS of the HOMO of the organic HTL is higher than that of the VB of MHP, we suggest that a slight band offset is beneficial for the device performance, so that V_{OC} can be maximized without compromising short-circuit current.

The new insights gained by our analysis reveal that an improvement of energy-level alignment and the quality of the MHP:HTL interface is crucial for achieving higher V_{OC} for solar cells incorporating wide-bandgap mixed-halide MHPs. Recent studies illustrated that the replacement of PTAA with self-assembled monolayers (SAMs) can minimize the V_{OC} losses associated with the MHP:HTL interface by 63 mV for devices based on for 1.6 and 1.8 eV-bandgap perovskites.[11c,13b,14a] This improvement can be attributed to better energetic alignment and fewer defects being present at the MHP:HTL interface. However, the HOMOs of such SAMs are currently still better optimized for the 1.6 eV bandgap perovskites,[14a] equivalent to x = 0 bromide content for the series of MHPs examined here. Therefore, we conclude that an improvement in the V_{OC} of wide-bandgap perovskites would require the development of novel HTLs with HOMO levels better matching the VBM of respective MHPs. We note that other than such energetic considerations, novel HTLs should have minimal interfacial defects (e.g., offered by SAMs molecules) and wide bandgaps to minimize parasitic absorption while also efficiently blocking electron transfer.[14a]

3. Conclusion

In conclusion, we have identified and quantified the non-radiative loss mechanisms associated with the interface formed between mixed-halide perovskites and hole extraction layers, through application of a full dynamical model to time-resolved photoluminescence transients. By tuning the energetic alignment between the valence band maximum of $FA_{0.83}Cs_{0.17}Pb(I_{1-x}Br_x)_3$ metal halide perovskite (MHP) and the highest occupied molecular orbital (HOMO) of the commonly implemented hole extraction material PTAA through changes in bromide content (x) between x = 0 to x = 1, we have been able to assign and disentangle all relevant processes affecting charge-carrier dynamics in such half-stacks. Comparison of such dynamics with those recorded for corresponding MHPs coated with an inert PMMA layer further allowed us to identify the processes directly arising from the electronically active MHP:PTAA interface. We show that interfacial losses increase with increasing energy-level misalignment primarily because of hole accumulation in the HOMO of the PTAA, followed by subsequent across-interfacial recombination. With an increasing energetic barrier, holes in the HOMO of PTAA are unable to return to the VBM of the MHP, ultimately leading to substantial across-interfacial recombination between the electrons in the conduction band of the MHP with holes accumulated in the HOMO of the PTAA.

We further showed that the assignment of "early" and "late" components in such commonly examined TRPL traces can be too simplistic under certain circumstances. For example, our dynamical model revealed that while the early TRPL lifetime can be dominated by hole transfer and the late TRPL lifetime by across-interfacial recombination, such assignments may no longer be valid when the total density of defects becomes too high. In this case of high defect density, both early and late TRPL dynamics would ultimately be dominated by the defect-assisted non-radiative recombination within MHP itself rather than non-radiative losses at the MHP:HTL interface. We further established that the amplitude of the late TRPL dynamic is usually determined by the amount of hole accumulation in the HOMO of PTAA.

Finally, we examined the extent to which a hypothetical HTL exhibiting ideal energy-level alignment that minimizes hole accumulation and low recombination at the MHP:HTL interface could improve the performance of photovoltaic devices incorporating the wide-bandgap MHPs. We show that Voc loss mainly originates from the interface between the perovskite and the PTAA and its magnitude increases with increasing energy-level misalignment. For x > 0.6, the Voc loss from defects starts to become more significant while Voc loss caused by the interface is still the dominant factor. We, therefore, conclude by stressing the importance of the development of new HTLs specifically designed for wide-bandgap perovskites that are critical to the success of high-efficiency tandem perovskite solar cells. In addition, they should introduce minimal interfacial defects and possess wide bandgaps to minimize parasitic absorption while also efficiently blocking electron transfer. If HTLs can be implemented according to these design criteria, ultra-high efficiency multi-junction perovskite solar cells will make an important leap toward becoming a renewable technology.

4. Experimental Section

Sample Fabrication: The perovskite precursor chemicals were purchased from the following suppliers: lead iodide (PbI_2, 99.99%) was purchased from TCI; lead bromide ($PbBr_2$, 98+%), cesium iodide (CsI, 99.999%) and cesium bromide (CsBr, 99.9%) were purchased from Alfa Aesar; formamidinium iodide (FAI, >99.99%) and formamidinium bromide (FABr, >99.99%) were purchased from Greatcell Solar. PTAA (Poly[bis(4-phenyl)(2,4,6-trimethylphenyl)amine, MW = 13,000 g mol^{-1}) was purchased from Flexink. PMMA (Poly(methyl methacrylate), MW = 15,000 g mol^{-1}) was purchased from Sigma Aldrich. All solvents in this work were purchased from Sigma Aldrich. $FA_{0.83}Cs_{0.17}PbI_3$ was formed by weighing CsI, FAI, PbI_2 stoichiometrically in an N_2 filled glovebox. Similarly, $FA_{0.83}Cs_{0.17}PbBr_3$ was formed by weighing CsBr, FABr, $PbBr_2$ stoichiometrically in an N_2 filled glovebox. To each, an appropriate volume of 4:1 DMF (dimethylformamide): DMSO (dimethyl sulfoxide) was added to achieve a nominal concentration of 0.6 M. Each solution was stirred overnight. To achieve intermediary bromide ratios, appropriate volumes of each of these solutions were mixed. PTAA and PMMA were dissolved in chlorobenzene at concentrations of 80 and 100 mg mL^{-1} respectively. Circular (diameter = 13 mm) z-cut quartz substrates were purchased from UQG optics. Before deposition, the following cleaning procedure was undertaken. The substrates were sequentially sonicated for at least 15 min in 1 vol.% Decon90 in deionized water, acetone, and isopropanol. Following the final sonication, the substrates were dried with a N_2 gun. The substrates were then treated with a UV-ozone plasma for 15 min before being immediately transferred into an N_2 filled glovebox where the perovskite thin films and polymer layers were deposited. To form the perovskite thin films, the following spin-coating procedure was used. 50 µL of perovskite precursor was dynamically deposited onto the substrate spinning at 1000 rpm. After 5 s, the substrate was accelerated at a rate of 800 rpm s^{-1} to a final speed of 5000 rpm for 30 s. An antisolvent quench was performed by depositing 50 µL of anisole at optimized times (see Table S1 in Supporting Information) before the end of the spin-coating cycle for each bromide ratio. Following the spin-coating procedure, the perovskite thin films were annealed for 1 h at 100 °C. After annealing, the samples were allowed to return to ambient temperature (≈25 °C). Either polymer layer was applied by depositing 60 µL on a static substrate. The substrate was then accelerated to 2000 rpm for 30s. The samples were then annealed for 5 min.

X-ray Diffraction Measurements: The X-ray diffraction (XRD) patterns were measured in air using a Panalytical X'pert powder diffractometer with a copper X-ray source (Cu-Kα X-rays with a wavelength of 1.5418 Å). The scan range was from 5.0 to 60.0 ° and the scan step size was set as 0.004 °. The raw XRD patterns were then corrected for tilt by shifting the 2θ-axis to the z-cut quartz reference peak, which is at 2θ = 16.433 and 33.172 °.[46] The baseline was corrected to a flat line by using the asymmetrically weighted penalized least squares smoothing algorithm.[47]

Absorptions: Reflectance (R) and transmittance (T) spectra were measured using a Fourier transform infrared (FTIR) spectrometer (Bruker vertex 80v), configured with a tungsten halogen lamp illumination source, a CaF_2 beamsplitter, and a silicon diode detector. The absorption coefficient (α) spectra were calculated as $\alpha = -\frac{1}{d} \cdot \log_{10}(\frac{T}{1-R})$ where d is the film thickness.

Steady-State Photoluminescence Measurements: The thin films were photo-excited with a 470 nm diode laser (Picoquant LDH-D-C-470) with a 1 MHz repetition rate at a fluence of 76.2 nJ cm^{-2}. The resultant photoluminescence (PL) was collected and coupled to a grating spectrometer (Princeton Instruments, SP-2558), which directed the spectrally dispersed PL onto a silicon iCCD (intensified charge-coupled device, PI-MAX4, Princeton Instruments). A glass color filter (495 GY 50 long pass) was used to block the laser scatter. A Keysight Technologies 33600A Trueform waveform generator was used to synchronize the sample excitation and PL collection time. The gate width was set as 1 µs to integrate the PL for each excitation before the next pulse arrived. The thin films were mounted in a vacuum cell under low pressure (≈10^{-2} mbar). The steady-state PL spectra were unconventionally collated under pulsed excitation as

time-integrated spectra to directly compare the time-resolved PL to steady-state PL collected under the same excitation conditions. However, steady-state PL measurements were also recorded following excitation with continuous waves at a power density of 255.9 mW cm^{-2} to verify that the steady-state PL trends across Br contents remain identical regardless of the laser repetition rate. Each PL spectrum was spectrally corrected with an OL245M irradiance standard tungsten lamp and background-corrected by a spectrum recorded without laser excitation. To account for the spot-to-spot variation of spin-coated thin films, 3 different spots were measured for each thin film. The full width at half maxima (FWHM) of the PL spectra were calculated from sigma (σ) obtained using a Gaussian function $f(x; A, \mu, \sigma) = \frac{A}{\sigma\sqrt{2\pi}} e^{\frac{-(x-\mu)^2}{2\sigma^2}}$ where A is the amplitude, μ is the centre, σ is the sigma width. The FWHM is calculated as $2\sigma\sqrt{2\ln 2}$.

Time-Resolved Photoluminescence Measurements: The charge-carrier dynamics were investigated by using time-resolved PL measurements based on the time-correlated single photon counting (TCSPC) technique. A 470 nm diode laser (Picoquant LDH-D-C-470) was used to photo-excite the samples with 1 MHz repetition rate at 13.4, 33.5, and 76.2 nJ cm^{-2}. The resultant photoluminescence (PL) was collected and coupled to a grating spectrometer (Princeton Instruments, SP-2558), which directed the spectrally dispersed PL onto a photon-counting detector (PDM series from MPD). A glass color filter (495 GY 50 long pass) was used to block the laser scatter. Timing was controlled by a PicoHarp300 TCSPC event timer connected to an external trigger (Keysight Technologies 33600A Trueform waveform generator). Time-correlated single photon counting (TCSPC) decays were measured at the initial PL peak of the mixed phase before any significant halide segregation had occurred. The thin films were mounted in a vacuum cell under low pressure ($\approx 10^{-2}$ mbar). In order to prevent halide segregation, each TCSPC measurement was limited to only 1 min acquisition for each measurement. In order to verify that no significant halide segregation had affected the measurements, steady-state PL spectra were measured before and after each TCSPC measurement. To account for the spot-to-spot variation of spin-coated thin films, 3 different spots were measured for each thin film. To minimize the human error arising from switching software between LightField (steady-state PL) and PicoHarp (TCSPC) and switching of the exit port of the grating spectrometer, the PL and TCSPC acquisitions for each spot were fully automated with a python script. Moreover, both front (from either PMMA or PTAA side) and the back side (quartz side) excitation configurations were measured to consider the possible difference in charge-carrier dynamics owing to diffusion and different surface morphologies on each side of the film stacks. To enhance signal to noise ratio of the TRPL spectra, the TRPL spectra of the same bromide content measured at different spots and sides were added. Each PL and TCSPC spectrum were spectrally corrected with an OL245M irradiance standard tungsten lamp and background-corrected with the laser excitation turned off.

Supporting Information

Supporting Information is available from the Wiley Online Library or from the author.

Acknowledgements

The authors acknowledge the Engineering and Physical Sciences Research Council (EPSRC), UK, for financial support, e.g., through grant no. EP/S004947/1. L.M.H. acknowledges support through a Hans Fischer Senior Fellowship from the Technical University of Munich's Institute for Advanced Study, funded by the German Excellence Initiative.

Conflict of Interest

Henry Snaith is cofounder and CSO of Oxford PV Ltd, a company commercializing perovskite PV technology.

Data Availability Statement

The data that support the findings of this study are available from the corresponding author upon reasonable request.

Keywords

band alignment, charge carrier dynamics, hole transport layers, mixed halide perovskites, open circuit voltage, transient photoluminescence, wide-bandgap

Received: February 8, 2024
Revised: March 19, 2024
Published online: April 3, 2024

[1] NREL, N.R.E.L. B. Research Cell Efficiency Chart, https://www.nrel.gov/pv/assets/pdfs/best-research-cell-efficiencies.pdf, (accessed: March 2024)
[2] M. A. Green, A. Ho-Baillie, H. J. Snaith, *Nat. Photonics* **2014**, *8*, 506.
[3] S. D. Wolf, J. Holovsky, S.-J. Moon, P. Löper, B. Niesen, M. Ledinsky, F.-J. Haug, J.-H. Yum, C. Ballif, *J. Phys. Chem. Lett.* **2014**, *5*, 1035.
[4] A. Miyata, A. Mitioglu, P. Plochocka, O. Portugall, J. T.-W. Wang, S. D. Stranks, H. J. Snaith, R. J. Nicholas, *Nat. Phys.* **2015**, *11*, 582.
[5] C. Wehrenfennig, G. E. Eperon, M. B. Johnston, H. J. Snaith, L. M. Herz, *Adv. Mater.* **2014**, *26*, 1584.
[6] X. Zhang, M. E. Turiansky, J.-X. Shen, C. G. V. d. Walle, *J. Appl. Phys.* **2022**, *131*, 090901.
[7] S. D. Stranks, G. E. Eperon, G. Grancini, C. Menelaou, M. J. P. Alcocer, T. Leijtens, L. M. Herz, A. Petrozza, H. J. Snaith, *Science* **2013**, *342*, 341.
[8] D. P. McMeekin, G. Sadoughi, W. Rehman, G. E. Eperon, M. Saliba, M. T. Hörantner, A. Haghighirad, N. Sakai, L. Korte, B. Rech, M. B. Johnston, L. M. Herz, H. J. Snaith, *Science* **2016**, *351*, 151.
[9] a) M. H. Futscher, B. Ehrlerm, *ACS Energy Lett.* **2016**, *1*, 863; b) A. J. Ramadan, R. D. J. Oliver, M. B. Johnston, H. J. Snaith, *Nat. Rev. Mater.* **2023**, *8*, 822.
[10] W. Shockley, H. J. Queisser, *J. Appl. Phys.* **1960**, *32*, 510.
[11] a) K. Suchan, T. J. Jacobsson, C. Rehermann, E. L. Unger, T. Kirchartz, C. M. Wolff, *Adv. Energy Mater.* **2023**, *14*, 2303420; b) S. Mahesh, J. M. Ball, R. D. J. Oliver, D. P. McMeekin, P. K. Nayak, M. B. Johnston, H. J. Snaith, *Energy Environ. Sci.* **2020**, *13*, 258; c) P. Caprioglio, J. A. Smith, R. D. J. Oliver, A. Dasgupta, S. Choudhary, M. D. Farrar, A. J. Ramadan, Y.-H. Lin, M. G. Christoforo, J. M. Ball, J. Diekmann, J. Thiesbrummel, K.-A. Zaininger, X. Shen, M. B. Johnston, D. Neher, M. Stolterfoht, H. J. Snaith, *Nat. Commun.* **2023**, *14*, 932.
[12] a) F. Peña-Camargo, P. Caprioglio, F. Zu, E. Gutierrez-Partida, C. M. Wolff, K. Brinkmann, S. Albrecht, T. Riedl, N. Koch, D. Neher, M. Stolterfoht, *ACS Energy Lett.* **2020**, *5*, 2728; b) E. T. Hoke, D. J. Slotcavage, E. R. Dohner, A. R. Bowring, H. I. Karunadasa, M. D. McGehee, *Chem. Sci.* **2015**, *6*, 613; c) S. G. Motti, J. B. Patel, R. D. J. Oliver, H. J. Snaith, M. B. Johnston, L. M. Herz, *Nat. Commun.* **2021**, *12*, 6955; d) V. J.-Y. Lim, A. J. Knight, R. D. J. Oliver, H. J. Snaith, M. B. Johnston, L. M. Herz, *Adv. Funct. Mater.* **2022**, *32*, 2204825; e) A. J. Knight, A. D. Wright, J. B. Patel, D. P. McMeekin, H. J. Snaith, M. B. Johnston, L. M. Herz, *ACS Energy Lett.* **2019**, *4*, 75; f) K. Datta, B. T. v. Gorkom, Z. Chen, M. J. Dyson, T. P. A. v. d. Pol, S. C. J. Meskers, S. Tao, P. A. Bobbert, M. M. Wienk, R. A. J. Janssen, *ACS Appl. Energy Mater.* **2021**, *4*, 6650; g) E. L. Unger, L. Kegelmann, K. Suchan, D. Sörell, L. Korte, S. Albrecht, *J. Mater. Chem. A* **2017**, *5*, 11401; h) Y. Guo, X. Yin, J. Liu, W. Que, *Matter* **2022**, *5*, 2015.
[13] a) H. Chen, A. Maxwell, C. Li, S. Teale, B. Chen, T. Zhu, E. Ugur, G. Harrison, L. Grater, J. Wang, Z. Wang, L. Zeng, S. M. Park, L. Chen,

P. Serles, R. A. Awni, B. Subedi, X. Zheng, C. Xiao, N. J. Podraza, T. Filleter, C. Liu, Y. Yang, J. M. Luther, S. D. Wolf, M. G. Kanatzidis, Y. Yan, E. H. Sargent, *Nature* **2023**, *613*, 676; b) Z. Yi, W. Wang, R. He, J. Zhu, W. Jiao, Y. Luo, Y. Xu, Y. Wang, Z. Zeng, K. Wei, J. Zhang, S.-W. Tsang, C. Chen, W. Tang, D. Zhao, *Energy Environ. Sci.* **2024**, *17*, 202; c) Y. Zhao, C. Wang, T. Ma, L. Zhou, Z. Wu, H. Wang, C. Chen, Z. Yu, W. Sun, A. Wang, H. Huang, B. Zou, D. Zhao, X. Li, *Energy Environ. Sci.* **2023**, *16*, 2080; d) S. Mariotti, E. Köhnen, F. Scheler, K. Sveinbjörnsson, L. Zimmermann, M. Piot, F. Yang, B. Li, J. Warby, A. Musiienko, D. Menzel, F. Lang, S. Keßler, I. Levine, D. Mantione, A. Al-Ashouri, M. Härtel, K. Xu, A. Cruz, J. Kurpiers, P. Wagner, H. Köbler, J. Li, A. Magomedov, D. Mecerreyes, E. Unger, A. Abate, M. Stolterfoht, B. Stannowski, R. Schlatmann, et al., *Science* **2023**, *381*, 63; e) C. Liu, Y. Yang, H. Chen, J. Xu, A. Liu, A. S. R. Bati, H. Zhu, L. Grater, S. S. Hadke, C. Huang, V. K. Sangwan, T. Cai, D. Shin, L. X. Chen, M. C. Hersam, C. A. Mirkin, B. Chen, M. G. Kanatzidis, E. H. Sargent, *Science* **2023**, *382*, 810; f) F. Ye, S. Zhang, J. Warby, J. Wu, E. Gutierrez-Partida, F. Lang, S. Shah, E. Saglamkaya, B. Sun, F. Zu, S. Shoaee, H. Wang, B. Stiller, D. Neher, W.-H. Zhu, M. Stolterfoht, Y. Wu, *Nat. Commun.* **2022**, 13, 7454; g) J. Liu, M. D. Bastiani, E. Aydin, G. T. Harrison, Y. Gao, R. R. Pradhan, M. K. Eswaran, M. Mandal, W. Yan, A. Seitkhan, M. Babics, A. S. Subbiah, E. Ugur, F. Xu, L. Xu, M. Wang, A. u. Rehman, A. Razzaq, J. Kang, R. Azmi, A. A. Said, F. H. Isikgor, T. G. Allen, D. Andrienko, U. Schwingenschlögl, F. Laquai, S. D. Wolf, *Science* **2022**, *377*, 302; h) Q. Jiang, J. Tong, R. A. Scheidt, X. Wang, A. E. Louks, Y. Xian, R. Tirawat, A. F. Palmstrom, M. P. Hautzinger, S. P. Harvey, S. Johnston, L. T. Schelhas, B. W. Larson, E. L. Warren, M. C. Beard, J. J. Berry, Y. Yan, K. Zhu, *Science* **2022**, *378*, 1295.

[14] a) A. Al-Ashouri, A. Magomedov, M. Roß, M. Jos˘t, G. Chistiakova, T. Bertram, M. Talaikis, E. Ko¨hnen, E. Kasparavic˘ius, S. Levcenco, J. A. Ma´rquez, L. n. Gil-Escrig, C. J. Hages, R. Schlatmann, B. Rech, T. Malinauskas, T. Unold, C. A. Kaufmann, L. Korte, G. Niaura, V. Getautis, S. Albrecht, *Energy Environ. Sci.* **2019**, *12*, 3356; b) M. Stolterfoht, P. Caprioglio, C. M. Wolff, J. A. Marquez, J. Nordmann, S. Zhang, D. Rothhardt, U. Hormann, Y. Amir, A. Redinger, L. Kegelmann, F. Zu, S. Albrecht, N. Koch, T. Kirchartz, M. Saliba, T. Unold, D. Neher, *Energy Environ. Sci.* **2019**, *12*, 2778.

[15] J. Wang, L. Zeng, D. Zhang, A. Maxwell, H. Chen, K. Datta, A. Caiazzo, W. H. M. Remmerswaal, N. R. M. Schipper, Z. Chen, K. Ho, A. Dasgupta, G. Kusch, R. Ollearo, L. Bellini, S. Hu, Z. Wang, C. Li, S. Teale, L. Grater, B. Chen, M. M. Wienk, R. A. Oliver, H. J. Snaith, R. A. J. Janssen, E. H. Sargent, *Nat. Energy* **2024**, *9*, 70.

[16] a) A. Al-Ashouri, E. Köhnen, B. Li, A. Magomedov, H. Hempel, P. Caprioglio, J. A. Márquez, A. B. M. K. Vilches Ernestas, J. A. Smith, N. Ernestas, N. Phung, D. Menzel, M. Grischek, L. Kegelmann, D. Skroblin, C. Gollwitzer, T. Malinauskas, M. Jošt, G. Matic, B. Rech, R. Schlatmann, M. Topic, L. Korte, A. Abate, B. Stannowski, D. Neher, M. Stolterfoht, T. Unold, V. Getautis, S. Albrecht, *Science* **2020**, *370*, 1300; b) I. Gelmetti, N. r. F. Montcada, A. Pérez-Rodríguezc, E. Barrena, C. Ocalc, I. s. García-Benitod, A. n. Molina-Ontoriad, N. Martínd, A. Vidal-Ferrana, E. Palomaresa, *Energy Environ. Sci.* **2019**, *12*, 1309; c) R. D. J. Oliver, P. Caprioglio, F. pen ã-Camargo, L. R. V. Buizza, F. Zu, A. J. Ramadan, S. G. Motti, S. Mahesh, M. M. McCarthy, J. H. Warby, Y.-H. Lin, N. Koch, S. Albrecht, L. M. Herz, M. B. Johnston, D. Neher, M. Stolterfoht, H. J. Snaith, *Energy Environ. Sci.* **2022**, *15*, 714.

[17] S. Prathapani, P. Bhargava, S. Mallick, *Appl. Phys. Lett.* **2018**, *112*, 092104.

[18] J. Endres, M. Kulbak, L. Zhao, B. P. Rand, D. Cahen, G. Hodes, A. Kahn, *J. Appl. Phys.* **2017**, *121*, 035304.

[19] D. Bryant, N. Aristidou, S. Pont, I. Sanchez-Molina, T. Chotchunangatchaval, S. Wheeler, J. R. Durrant, S. A. Haque, *Energy Environ. Sci.* **2016**, *9*, 1655.

[20] a) J. Endres, D. A. Egger, M. Kulbak, R. A. Kerner, L. Zhao, S. H. Silver, G. Hodes, B. P. Rand, D. Cahen, L. Kronik, A. Kahn, *J. Phys. Chem. Lett.* **2016**, *7*, 2722; b) S. Tao, I. Schmidt, G. Brocks, J. Jiang, I. Tranca, K. Meerholz, S. Olthof, *Nat. Commun.* **2019**, *10*, 10; c) K. T. Butler, J. M. Frost, A. Walsh, *Mater. Horiz.* **2015**, *2*, 228. d) B. Philippe, T. J. Jacobsson, J.-P. Correa-Baena, N. K. Jena, A. Banerjee, S. Chakraborty, U. B. Cappel, R. Ahuja, A. Hagfeldt, M. Odelius, H. k. Rensmo, *J. Phys. Chem. C* **2017**, *121*, 26655; e) C. Li, J. Wei, M. Sato, H. Koike, Z.-Z. Xie, Y.-Q. Li, K. Kanai, S. Kera, N. Ueno, J.-X. Tang, *ACS Appl. Mater. Interfaces* **2016**, *8*, 11526.

[21] Y. Chen, S. G. Motti, R. D. J. Oliver, A. D. Wright, H. J. Snaith, M. B. Johnston, L. M. Herz, M. R. Filip, *J. Phys. Chem. Lett.* **2022**, *13*, 4184.

[22] a) L. M. Herz, *ACS Energy Lett.* **2017**, *2*, 1539; b) A. D. Wright, C. Verdi, R. L. Milot, G. E. Eperon, M. A. Pérez-Osorio, H. J. Snaith, F. Giustino, M. B. Johnston, L. M. Herz, *Nat. Commun.* **2016**, *7*, 11755.

[23] W. Rehman, D. P. McMeekin, J. B. Patel, R. L. Milot, M. B. Johnston, H. J. Snaith, L. M. Herz, *Energy Environ. Sci.* **2017**, *10*, 361.

[24] U. Rau, *Phys. Rev. B* **2007**, *76*, 085303.

[25] a) D. J. Slotcavage, H. Karunadasa, M. D. McGehee, *ACS Energy Lett.* **2016**, *1*, 1199; b) A. J. Barker, A. Sadhanala, F. Deschler, M. Gandini, S. P. Senanayak, P. M. Pearce, E. Mosconi, A. J. Pearson, Y. Wu, A. R. S. L. Kandada, Tomas, F. D. A, S. E. Dutton, A. Petrozza, R. H. Friend, *ACS Energy Lett.* **2017**, *2*, 1416; c) C. G. Bischak, C. L. Hetherington, H. Wu, S. Aloni, D. F. Ogletree, D. T. Limmer, N. S. Ginsberg, *Nano Lett.* **2017**, *17*, 1028; d) A. J. Knight, L. M. Herz, *Energy Environ. Sci.* **2020**, *13*, 2024.

[26] L. M. Herz, *Rev. Phys. Chem.* **2016**, *67*, 65.

[27] Y. Li, B. Wang, T. Liu, Q. Zeng, D. Cao, H. Pan, G. Xing, *ACS Appl. Mater. Interfaces* **2022**, *14*, 3284.

[28] a) E. M. Hutter, T. Kirchartz, B. Ehrier, D. Cahen, E. v. Hauff, *Appl. Phys. Lett.* **2020**, *116*, 6; b) J. Warby, F. Zu, S. Zeiske, E. Gutierrez-Partida, L. Frohloff, S. Kahmann, K. Frohna, E. Mosconi, E. Radicchi, F. Lang, S. Shah, F. Peña-Camargo, H. Hempel, T. Unold, N. Koch, A. Armin, F. De Angelis, S. D. Stranks, D. Neher, M. Stolterfoht, *Adv. Energy Mater.* **2022**, *12*, 2103567.

[29] J. Wang, W. Fu, S. Jariwala, I. Sinha, A. K.-Y. Jen, D. S. Ginger, *ACS Energy Lett.* **2019**, *4*, 222.

[30] A. B. Sproul, *J. Appl. Phys.* **1994**, *76*, 2851.

[31] a) B. Krogmeier, F. Staub, D. Grabowski, U. Rau, T. Kirchartz, *Sustainable Energy Fuels* **2018**, *2*, 1027; b) J. Haddad, B. Krogmeier, B. Klingebiel, L. Krückemeier, S. Melhem, Z. Liu, J. Hüpkes, S. Mathur, T. Kirchartz, *Adv. Mater. Interfaces* **2020**, *7*, 2000366; c) L. Kruckemeier, B. Krogmeier, Z. Liu, U. Rau, T. Kirchartz, *Adv. Energy Mater.* **2021**, *11*, 19.

[32] E. M. Hutter, J.-J. Hofman, M. L. Petrus, M. Moes, R. D. Abellon, P. Docampo, T. J. Savenije, *Adv. Energy Mater.* **2017**, *7*, 1602349.

[33] C. Ding, Y. Zhanga, F. Liua, Y. Kitabatakeb, S. Hayasec, T. Toyoda, K. Yoshinod, T. Minemotoe, K. Katayamab, Q. Shena, *Nano Energy* **2018**, *53*, 17.

[34] a) I. Levine, A. Al-Ashouri, A. Musiienko, H. Hempel, A. Magomedov, A. Drevilkauskaite, V. Getautis, D. Menzel, K. Hinrichs, T. Unold, S. Albrecht, T. Dittrich, *Joule* **2021**, *5*, 2915. b) E. Ugur, J. I. Khan, E. Aydin, M. Wang, M. Kirkus, M. Neophytou, I. McCulloch, S. D. Wolf, F. Laquai, *J. Phys. Chem. Lett.* **2019**, *10*, 6921.

[35] a) R. A. Marcus, *J. Chem. Phys.* **1956**, *24*, 966; b) Z. Shuai, W. Li, J. Ren, Y. Jiang, H. Geng, *J. Chem. Phys.* **2020**, *153*, 0800902.

[36] a) J. Jortner, *J. Chem. Phys.* **2008**, *64*, 4860; b) J. Mooney, M. M. Krause, J. I. Saari, P. Kambhampati, *Phys. Rev. B* **2013**, *87*, 081201.

[37] a) H. Zhu, Y. Yang, K. Hyeon-Deuk, M. Califano, N. Song, Y. Wang, W. Zhang, O. V. Prezhdo, T. Lian, *Nano Lett.* **2014**, *14*, 1263; b) Z. Yin, J. Leng, S. Wang, G. Liang, W. Tian, K. Wu, S. Jin, *J. Am. Chem. Soc.* **2021**, *143*, 4725.

[38] M. Righetto, S. S. Lim, D. Giovanni, J. W. M. Lim, Q. Zhang, S. Ramesh, Y. K. E. Tay, T. C. Sum, *Nat. Commun.* **2020**, *11*, 2712.

[39] a) L. R. V. Buizza, A. D. Wright, G. Longo, H. C. Sansom, C. Q. Xia, M. J. Rosseinsky, M. B. Johnston, H. J. Snaith, L. M. Herz, *ACS Energy Lett.* **2021**, *6*, 1729; b) A. D. Wright, L. R. V. Buizza, K. J. Savill, G. Longo, H. J. Snaith, M. B. Johnston, L. M. Herz, *J. Phys. Chem. Lett.* **2021**, *12*, 3352.

[40] M. T. Hö rantner, T. Leijtens, M. E. Ziffer, G. E. Eperon, M. G. Christoforo, M. D. McGehee, H. J. Snaith, *ACS Energy Lett.* **2017**, *2*, 2506

[41] a) X. Zhao, C. Yao, K. Gu, T. Liu, Y. Xia, Y.-L. Loo, *Energy Environ. Sci.* **2020**, *13*, 4334. b) E. V. Péan, S. Dimitrov, C. S. D. Castro, M. L. Davies, *Phys. Chem. Chem. Phys.* **2020**, *22*, 28345; c) Z. Li, J. Dong, C. Liu, J. Guo, L. Shen, W. Guo, *Nano -Micro Lett.* **2019**, *11*, 50; d) J. Tao, N. Ali, K. Chen, Z. Huai, Y. Sun, G. Fu, W. Kong, S. Yang, *J. Mater. Chem. A* **2019**, *7*, 1349. e) j. I. Khan, F. H. Isikgor, E. Ugur, W. Raja, G. T. Harrison, E. Yengel, T. D. Anthopoulos, S. D. Wolf, F. Laquai, *ACS Energy Lett.* **2021**, *6*, 4155.

[42] P. Caprioglio, M. Stolterfoht, C. M. Wolff, T. Unold, B. Rech, S. Albrecht, D. Neher, *Adv. Energy Mater.* **2019**, *9*, 1901631.

[43] a) D. Ompong, K. S. Ram, D. D. Y. H. Setsoafia, M. Rad, J. Singh, *Adv. Mater. Interfaces* **2023**, *10*, 2201578; b) F. Peña-Camargo, P. Caprioglio, F. Zu, E. Gutierrez-Partida, C. M. Wolff, K. Brinkmann, S. Albrecht, T. Riedl, N. Koch, D. Neher, M. Stolterfoht, *ACS Energy Lett.* **2020**, *5*, 2728; c) R. D. J. Oliver, Y.-H. Lin, A. J. Horn, C. Q. Xia, J. H. Warby, M. B. Johnston, A. J. Ramadan, H. J. Snaith, *ACS Energy Lett.* **2020**, *5*, 3336; d) M. Kramarenko, C. G. Ferreira, G. Martínez-Denegri, C. Sansierra, J. Toudert, J. Martorell, *Sol. RRL* **2020**, *4*, 1900554; e) D. Luo, R. Su, W. Zhang, Q. Gong, R. Zhu, *Nat. Rev. Mater.* **2020**, *5*, 44.

[44] G. Eperon, H. Snaith, M. Hoerantner, *Nat. Rev. Chem.* **2017**, *1*, 0095.

[45] P. F. Barbara, T. J. Meyer, M. A. Ratner, *J. Phys. Chem.* **1996**, *100*, 13148.

[46] K. A. Elmestekawy, A. D. Wright, K. B. Lohmann, J. Borchert, M. B. Johnston, L. M. Herz, *ACS Nano* **2022**, *16*, 9640.

[47] S.-J. Baek, A. Park, Y.-J. Ahn, J. Choo, *Analyst* **2015**, *140*, 250.